Breakup and Droplet Formation of Slurry Jets

John C. Ogg* and Joseph A. Schetz†
Virginia Polytechnic Institute and State University, Blacksburg, Virginia

Presented herein is an experimental and numerical investigation of the breakup and droplet formation of laminar liquid and slurry jets issuing into quiescent air. The slurry was a water liquid phase with glass beads of 0-37 μm diameter. A 0.7-mm-diam nozzle was vibrated in the axial direction with a shaker to regulate the breakup of the jet. The velocity of the jet was varied between 0.5 and 3 m/s, and the disturbance wavelength was varied between 3 and 6 jet diameters. Mass loadings from 10 to 50% were investigated. The growth of the surface disturbances was measured from photographs. A numerical code for solving the axisymmetric Navier-Stokes equations was modified by the addition of equations simulating particles in the flowfield. It was found that the presence of particles in the jet caused changes in the behavior of the jet. Breakup of the jet became less regular, and other, nonaxisymmetric, modes of surface disturbances often were prominent. The numerical code produced excellent predictions of all details of the behavior of the liquid jets. The formulation only considered axisymmetric flow, thus it was less successful for the slurry jets. For experimental cases where the nonaxisymmetric modes on the slurry jets were small, the predictions of the growth of the axisymmetric modes were good.

Nomenclature

a	= particle radius
B_n	= amplitude of sinusoidal disturbance
B	= $\lvert D-D_0 \rvert / D_0$
B_0	= initial amplitude of sinusoidal disturbance
C_D	= coefficient of drag
D_0	= initial diameter of jet
F	= time constant of momentum transfer
K_m	= momentum transfer effectiveness
l	= particle loading; distance along jet
P	= pressure
R	= radius of curvature
T,t	= time
$\bar{T}$	= nondimensional time
u,v	= radial and axial fluid velocity component, respectively
u_p,v_p	= radial and axial particle velocity, respectively
We	= Weber number
x,y	= radial and axial coordinate, respectively
λ	= spatial length of disturbance
μ	= fluid viscosity
υ	= fluid kinematic viscosity
ρ	= fluid density
ρ_p	= particle phase density
$\bar{\rho}$	= fluid material density
$\bar{\rho}_p$	= particle material density
σ	= fluid coefficient of surface tension

Introduction

THE desirability of slurry fuels for aerospace applications has long been recognized, but the problems of slurry injection and combustion have yet to be adequately resolved. The heating value per unit volume of boron is 137,010 kJ/l (Ref. 1), which is four times that of JP-4 liquid fuel. This increase in heat-per-unit-volume could effect a significant increase in range or decrease in size of a missile propulsion system. A possible method of using boron or other solid fuels for air-breathing engines is to mix finely pulverized solid fuel with liquid fuel to produce a slurry. The function of the liquid is to provide a vehicle to carry the solid and to sustain through its combustion sufficient temperature to ignite the solid constituent of the fuel. Another application for slurry fuels is pulverized coal as the solid constituent in oil to fuel gas turbine and internal combustion engines.

The fundamental nature of liquid fuel injection has received much attention and is now understood well enough to produce efficient liquid fuel air-breathing engines. In the present work, a numerical and experimental approach is taken to study the fundamental similarities and differences between the breakup of a liquid and a slurry jet. This work concentrates on the detailed behavior of the idealized case of laminar, lightly loaded slurry jets injected into quiescent air as a first step toward the much more complicated, highly loaded turbulent jet in a cross-flow case.

The laminar liquid jet has been extensively investigated analytically using approximate solutions, and recently, numerical solutions for simplified flow conditions have been found. A great many experimental investigations have also been performed. The earliest analysis of a liquid jet was published by Rayleigh[2] for a cylindrical column of inviscid liquid at rest or with uniform velocity with the surface initially deformed by a small spatial perturbation, as shown in Fig. 1. Rayleigh showed that small perturbations which deformed the cross section of the jet from a circle would not grow, but that certain axisymmetric perturbations would. The nondimensional length of the disturbance determined the rate of growth. For $\lambda/D_0 = 4.51$, the growth rate was maximum, and disturbance lengths less than the circumference of the jet would not grow. A concise presentation of the linear analysis is given in Ref. 3, including a treatment of the effect of viscosity. Several nonlinear perturbation analyses of infinite jets have been done. A clear precis is presented by Bogy.[4]

A numerical method with the vorticity stream function formulation of the Navier-Stokes equations was used by Shokoohi[5] to investigate the formation of satellite drops from liquid jets. This method succeeded in simulating the doubly infinite jet but had limited success in simulating a jet of finite length issuing from a nozzle.

The present work is an investigation into the breakup and subsequent droplet formation of laminar slurry jets issuing into quiescent air. The growth due to capillary forces of the

Presented as Paper 83-0067 at the AIAA 21st Aerospace Sciences Meeting, Reno, Nev., Jan. 10-13, 1983; received Nov. 23, 1983; revision received March 5, 1984.

*Graduate Student, Aerospace and Ocean Engineering Department; currently Assistant Professor, University of Kansas, Lawrence, Kansas. Member AIAA.

†Professor and Department Head, Aerospace and Ocean Engineering Department. Associate Fellow AIAA.

surface disturbances was measured from photographs. A numerical code for solving the Navier-Stokes equations developed by Los Alamos Scientific Laboratories was modified by the addition of equations simulating particles in the liquid flowfield. This was employed to calculate the time history of the shape of both liquid and slurry jets under the action of surface tension for comparison with the experimental observations.

Experimental Apparatus and Procedures

The apparatus for the experiments consisted of three systems: a slurry-producing and -metering system, photographic equipment, and a vibrator for perturbing the jet.

Two types of devices for producing the slurry were studied: a mixing tank with an agitator and an eductor. The mixing tank provided easy control and measurement of slurry mass loading, but the flow rate was difficult to measure because the slurry clogged the flowmeter. The eductor system (see Fig. 2) provided simple flow rate measurement. As the system was completely filled with liquid and slurry at all times, the volume flow rate of the liquid into the system was equal to the volume flow rate of slurry through the nozzle. The flow rate of the liquid was measured using a rotameter. High-velocity liquid is injected across the bottom of the tank which entrains the high-density slurry from the tank forming the lower density injectant slurry. The number of particles induced into the slurry could be controlled by changing the gap between the nozzle and the exit tube and/or balancing the liquid flow between the two control valves.

The slurry was fed through small tubing to the injector nozzle because the low-volume flow rates of slurry (about 1 ml/s) might allow separation of phases in large diameter tubing. For the same reason, only a small chamber was made above the nozzle. The nozzle was connected to an electric shaker which was driven by a sine wave generator. The frequency was monitored by a counter. A stroboscope was used to monitor the perturbation frequency and observe jet behavior.

The liquid carrier was supplied to the eductor from a tank which was pressurized at 27 atm. The solid phase was spherical glass beads of 0-37 μm diameter with a material density of 2.8-3.0 kg/m^3.

The photographs were taken with Polaroid Type 55 film. The lens had a 210-mm focal length set at a stop of 4.5 at a shutter speed of 1/50 s. All photographs were back-lighted using a ground glass screen and an electronic flash. At the minimum intensity setting of the flash, the duration was short enough to freeze the jet motion.

Numerical Investigation

The full, viscous equations of motion were required for the slurry jet to model the nonlinear effects of the free surface for large amplitudes as well as to model interactive forces between the liquid and solid phases. Also, in order to model both of these effects simultaneously, a numerical method was required. The numerical technique employed is an adaptation of the volume of fluid (VOF) method for calculating incompressible flowfields. This method was proposed by Harlow and Welch[6] and others. It is used here to solve the axisymmetric, unsteady, multiphase, laminar flowfield with free surfaces. The code used is an extended version of SOLA-VOF[7] from Los Alamos Scientific Laboratory. The changes incorporated include mainly the addition of equations which model the solid phase added to the liquid flow.

Additional terms which represent the forces exerted on the liquid phase by the particle phase were incorporated into the momentum equation as

$$\frac{\partial u}{\partial t}+\frac{\partial u^2}{\partial x}+\frac{\partial uv}{\partial y}+\frac{u^2}{x}=-\frac{1}{\rho}\frac{\partial P}{\partial x}+\nu\left[\nabla^2 u-\frac{u}{x^2}\right]$$

$$-K_m(\rho_p/\rho)F(u-u_p) \tag{1}$$

$$\frac{\partial v}{\partial t}+\frac{\partial uv}{\partial x}+\frac{\partial v^2}{\partial y}+\frac{uv}{x}=-\frac{1}{\rho}\frac{\partial P}{\partial y}+\nu[\nabla^2 v]$$

$$-K_m(\rho_p/\rho)F(v-v_p) \tag{2}$$

$$\frac{\partial u}{\partial x}+\frac{\partial v}{\partial y}+\frac{u}{x}=0 \tag{3}$$

The last term in each of the momentum equations represents the force exerted on the fluid by the particle phase.

The particles in the slurry are treated as a continuous, compressible, fluid-like phase cohabiting the volume with the liquid constituent of the slurry. The volume displaced by the particle phase is considered small when compared to the overall volume. Because of this, the density of the liquid phase is considered to be uniform throughout the flowfield and equal to the liquid phase material density. On the other hand, the local density of the particle phase changes as particles move through the flow. The density of the particle phase is much greater than the density of the liquid, therefore, the equations model a slurry of dense, small particles in a continuous fluid of relatively low density. The result is that the density of the liquid does not change, and the particle phase behaves similarly to a compressible fluid without a pressure term.[8]

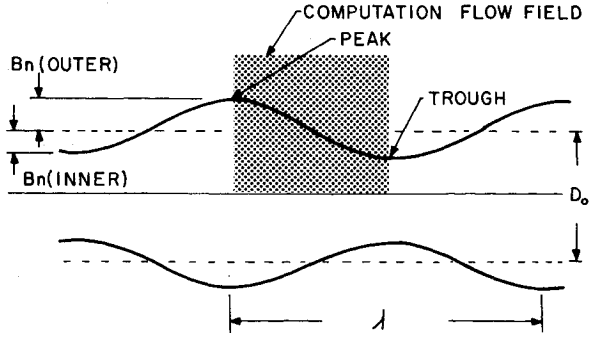

Fig. 1 Schematic of the jet showing the notation and the computational region.

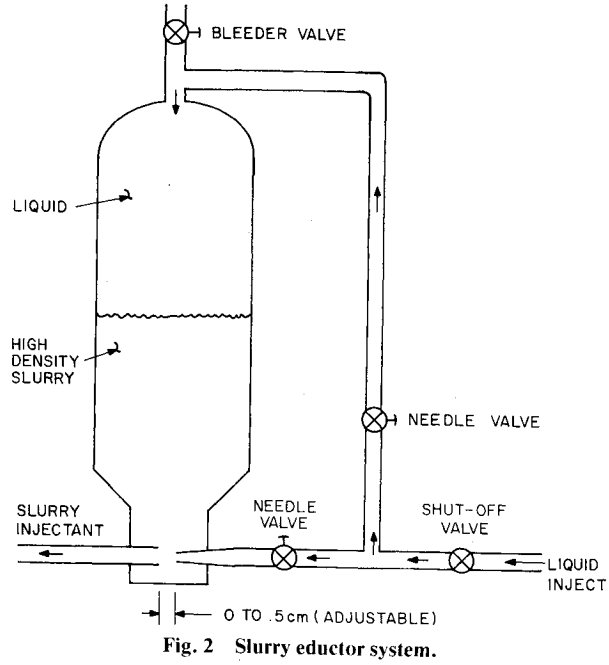

Fig. 2 Slurry eductor system.

If the particles are all the same size and sparsely distributed, then there is negligible interaction between particles. This means that the particle momentum equation is free of any viscous terms. For a slurry where the phases are as described above, the particle phase equations are

$$\frac{\partial(\rho_p u_p)}{\partial t}+\frac{\partial(\rho_p u_p{}^2)}{\partial x}+\frac{\partial(\rho_p u_p v_p)}{\partial y}+\frac{\rho_p u_p{}^2}{x}=\rho_p F(u-u_p) \tag{4}$$

$$\frac{\partial(\rho_p v_p)}{\partial t}+\frac{\partial(\rho_p u_p v_p)}{\partial x}+\frac{\partial(\rho_p v_p{}^2)}{\partial y}+\frac{\rho_p u_p v_p}{x}=\rho_p F(v-v_p) \tag{5}$$

$$\frac{\partial \rho_p}{\partial t}+\frac{\partial(\rho_p u_p)}{\partial x}+\frac{\partial(\rho_p v_p)}{\partial y}+\frac{\rho_p u_p}{x}=0 \tag{6}$$

Here, F is the particle time constant of momentum transfer due to the drag of the particle through the fluid phase expressed as [8]:

$$F=\frac{3}{8}C_D\frac{\bar{\rho}}{\bar{\rho}_p}\frac{1}{a}|u-u_p| \tag{7}$$

Using Stokes drag law

$$C_D=\frac{24}{Re}=\frac{24\mu}{2a|u-u_p|\bar{\rho}} \tag{8}$$

F becomes a constant based on the properties of the fluid phase and the particles

$$F=\frac{9}{2}\frac{\mu}{\bar{\rho}_p}\frac{1}{a^2} \tag{9}$$

The fact that F is a constant allows the component equations to become uncoupled, so that they may be solved independently. The effectiveness of momentum transfer K_m from the particles to the fluid is dependent on the proximity of particles to each other and their velocity relative to the fluid phase. This effectiveness is assumed to be unity for Stokes' flow.[8]

The fluid velocity components are defined on the boundaries of the computational cells to which they are normal. For example, $u_{i,j}$ is the velocity in the x direction defined on the right-hand side of cell i,j and $v_{i,j}$ the velocity in the y direction defined on the upper boundary of cell i,j. The velocity components defined on the left-hand side and the lower side are $u_{i-1,j}$ and $v_{i,j-1}$, respectively. The fluid properties such as pressure and density are defined at the center of each cell.

The differencing technique is an explicit, temporal marching scheme with an implicit evaluation of pressure and adjustment of velocity at each time step. The implicit step insures continuity of the flowfield.

The free surface location is computed from the volume fraction of fluid contained in each cell. In each partially full cell, there is a free surface. The orientation and position of the free surface is found by considering the volume fraction of fluid in the surrounding cells.

The boundary conditions imposed by the free surface are that of a free-slip surface with surface pressure. The surface pressure is calculated from the principal radii of curvature and the coefficient of surface tension σ, taken here as that of the liquid carrier.

The calculation procedure is as follows: Initial estimates of the velocity components for the flowfield are calculated explicitly from the momentum equations of the liquid phase. All of the flow variables used to calculate the new velocity components are those determined during the previous time step. After these initial approximations for the velocity have been made, the pressure is adjusted in each cell and the velocities are iteratively adjusted to satisfy local continuity.

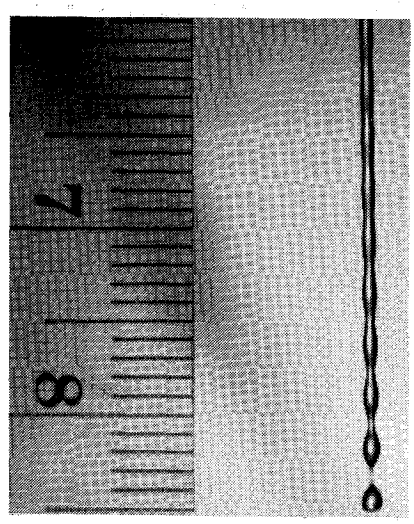

Fig. 3 Liquid jet; $V_0=330$ cm/s, $We=112$, $f=1200$ Hz, $\lambda/D_0=3.94$.

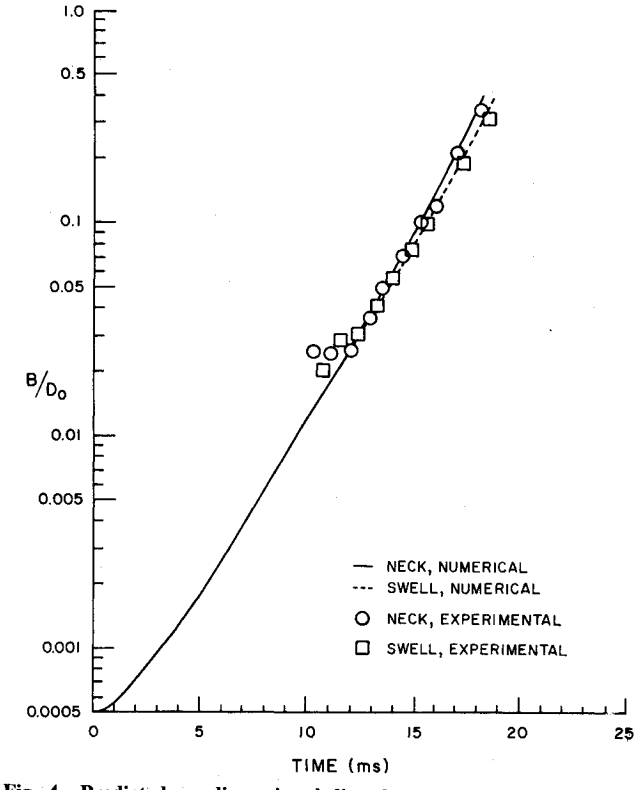

Fig. 4 Predicted nondimensional disturbance amplitude as a function of time compared to experimental results for liquid jets. Numerical prediction is for $\lambda/D_0=3.9$. The experimental conditions are the same as for Fig. 5, $\lambda/D_0=3.94$.

Next, the velocity components of the particle phase are explicitly calculated from particle momentum equations. These calculations are made using the updated values of the velocity components of the liquid phase. From the particle phase continuity equation, the new value of the particle phase density is calculated at each cell. Finally, the volume fraction of fluid in each cell is computed from the flux of fluid through the cell walls. This procedure constitutes one step forward in time.

The computational grid used was 16×16 cells, although fluid occupied less than 100 of these cells at any given time. The number of cells required to contain the fluid decreased as the fluid moved away from the centerline of the jet. The computational region is shown as the shaded area in Fig. 1.

The addition of the particle phase equations increased the computational time about 20%. Using a Fortan H extended

compiler, about 1h of CPU time on an IBM 3032 was required to calculate the formation of droplets from a slurry.

For the numerical cases the liquid kinematic viscosity was $1.006 \times 10^{-6} m^2/s$, the surface tension coefficient was 7.25×10^{-2} N/m, the density of the fluid phase was 1000 kg/m^3, the density of the solid phase was 3000 kg/m^3, the particle diameter used was 20 μm, and the jet diameter was 0.74 mm.

Results

Experiments

The first cases discussed are liquid jets, and two classes were investigated. The two classes are characterized in dimensionless terms by higher and lower Weber numbers (*We*). The range for the faster jets is from 98 to 163, and for the lower velocity jets from 15 to 37.

In Fig. 3, a high *We* jet is shown. The formation of drops from the perturbed liquid jet can be seen. The last incipient drop has been caught just before breakoff, and the drop at the bottom has broken off. The shape of the jet is nearly sinusoidal up to about 8 cm. As the necks become small, the disturbances take on a nonsinusoidal shape. Because of continuity, the mean diameter of the jet is also reduced as the wave amplitude increases. A jet such as this, when viewed with a synchronized strobe light, appears stationary. Each drop forms with perfect regularity at the same location as the preceding drop, and the form of each wave and drop is identical as it passes through a given location.

The jet surface is smooth and laminar, and the imposed disturbance is not sufficiently developed to be detected visually near the nozzle. On high *We* jets, the disturbance is too small to be seen for several centimeters downstream of the nozzle. The fact that the disturbance is not visible near the nozzle indicates that the initial disturbance is not a simple surface perturbation. The diameter of the jet is controlled mainly by the nozzle diameter and not by the vibration. The main effect of nozzle motion is to change the local jet velocity. These velocity disturbances then affect the local diameter of the jet by moving fluid into some regions and out of others. At some point, the pressure distribution induced by the surface shape and surface tension dominates the velocity of the fluid. When this happens, the growth of the disturbance shape becomes almost completely an effect of the surface tension and jet shape. The initial velocity disturbance soon is dominated by the velocity variations generated by surface tension effects. If the initial velocity disturbance is small, the initial velocity condition does not substantially alter the behavior of the jet from the behavior of a similar jet whose initial perturbation is a surface shape disturbance. The experiments were designed to minimize the velocity effects of the initial disturbances by keeping the oscillation amplitude at low levels. The slurry jets required larger amplitudes than the liquid jets to achieve regular breakup. In order to have the same initial conditions for both the liquid and the slurry jets, the disturbance amplitude used was the same for both cases.

Because the slurry jets, in particular, were susceptible to unrepeatable breakup due to small random background disturbances, the experiments were conducted near the wavelength of maximum initial disturbance growth rate as predicted by Rayleigh's linear analysis. In this wavelength region, the imposed disturbances could easily dominate other disturbances.

Figure 4 shows the measured growth of the jet "necks" and "swells" vs time for the case in Fig. 3. The curves labeled "numerical" predictions will be discussed later. The actual time was determined from the jet velocity and the distance to the location of interest, and the velocity of the jet was determined from the frequency of nozzle oscillation and the length of the disturbance on the jet. The time scale in this figure and all others is a relative time measured with respect to a shifted origin. This practice will be clarified later. The

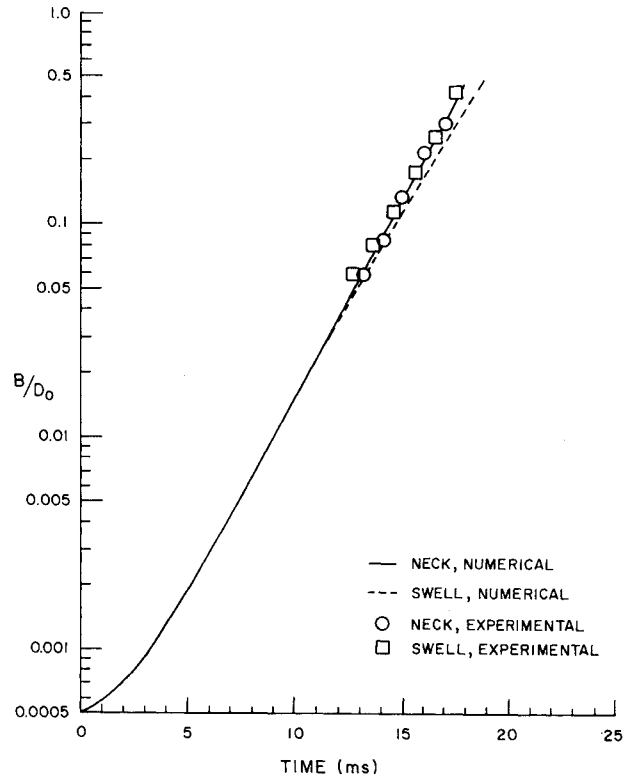

Fig. 5 Predicted nondimensional disturbance amplitude as a function of time compared to experimental results for a liquid jet. The numerical prediction is for $\lambda/D_0 = 4.51$. The experimental conditions are $W_e = 112$ and $\lambda/D_0 = 4.6$.

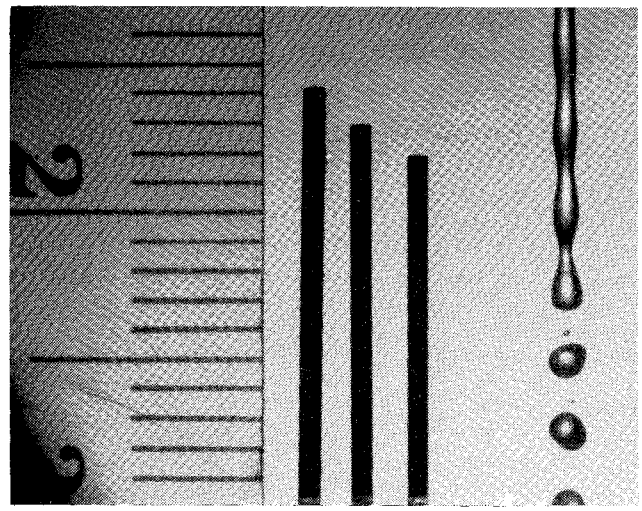

Fig. 6 Liquid jet; $V_0 = 124$ cm/s, $We = 12.7$, $f = 451$ Hz, $\lambda/D_0 = 3.8$.

measurements were made at the maximum and minimum diameters of the necks and swells, respectively, and these normally are at the center of the swell or neck. This is not so near the location of breakoff, where the minimum neck diameter moves downstream along the neck, and separation occurs nearer the drop. This can be seen on the last neck at the bottom of Fig. 3. Similarly, for the swell, the maximum diameter moves slightly downstream giving a nonsinusoidal asymmetry to the drop.

The exponential character of the growth is evident from the generally straight line form of the data on semilogarithmic paper. The growth rate of the swells at the earliest times is about the same as that of the necks. When the amplitude is greater than about 0.04, the growth of the swell lags the neck until breakoff. Below about 0.02-0.03, the data appear

scattered, but this is within the limits of accuracy of the measurements.

In Fig. 5, we show the disturbance growth results for a high *We* jet with an imposed disturbance wavelength equal to that predicted to have the largest initial growth rate by the linear Rayleigh analysis, $\lambda = 4.51/D_0$. As can be seen, the growth rate is almost perfectly exponential, i.e., with a nearly constant slope on semilog paper. The difference between the neck and swell growth rate is negligible except at a low disturbance amplitude.

Next, we consider a low *We* case as shown in Fig. 6. This jet has a similar wavelength-to-diameter ratio to that in Fig. 3. Because of the low velocity of this jet, a lower nozzle frequency is required to obtain the same dimensionless wavelength. The time between successive drops is 2.7 times greater on the low *We* jet than on the high *We* jet. This has an effect on the shape of the disturbance waveform. The waveform tends to deviate more away from the symmetry of the sinusoidal shape of an ideal infinite jet. Notice that in Fig. 6 the downstream region of the swell becomes larger than the upstream region. This can be understood by considering a single incipient drop bounded upstream and downstream by necks. The downstream neck is "older" than the upstream neck by the amount of time in one period of nozzle oscillation. The boundary conditions then on the two ends of the incipient drop are not the same at a given instant because the downstream neck is more developed due to its advanced age. The effect is stronger for jets with lower disturbance frequency than for jets with higher disturbance frequency because of the increased age differences between the necks for the jet with the lower frequency disturbance. This effect becomes more exaggerated the closer the incipient drop comes to breakoff, because, near breakoff, the growth rate is maximum, and the difference between the upstream and downstream necks is greatest.

Small satellite droplets may be seen between the main drops in Fig. 6. These occurred more frequently on low *We* jets than on high *We* jets.

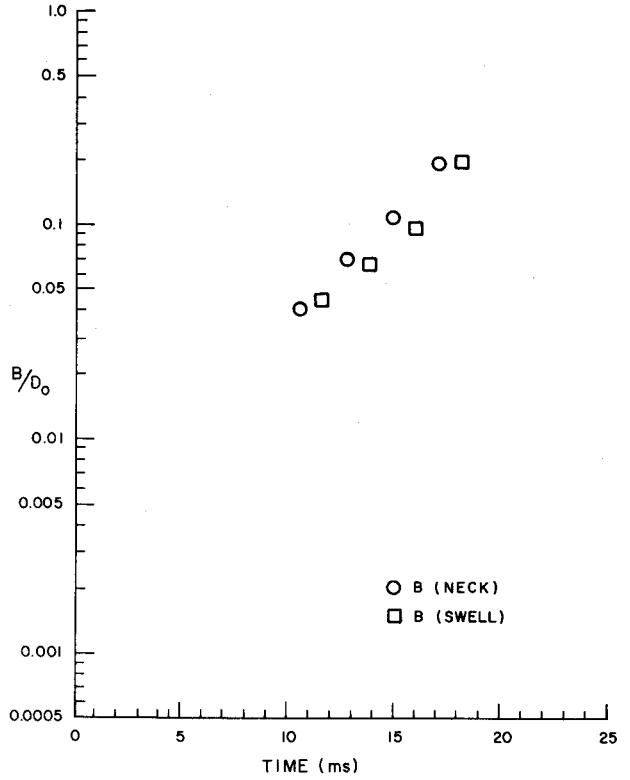

Fig. 7 Graph of the nondimensional disturbance amplitude as a function of time for a liquid jet, $V_0 = 124$ cm/s, $We = 12.7$, $f = 451$ Hz, $\lambda/D_0 = 3.8$.

In Fig. 7, the data taken from the jet in Fig. 6 are shown. The increased spacing between the data points is a result of the lower frequency of the nozzle vibration. The growth rate is slightly less than for the jet in Fig. 4 because λ/D_0 is farther from the value for maximum initial growth. In this case, the growth of the neck is nearly linear. On the other hand, the swell growth rate is increasing with time. Near breakoff, the growth rate of the swells has increased beyond that of the necks and is approaching the rate shown in Fig. 4.

For the slurry jets, two types are to be discussed again: fast jets with *We* from 130 to 160 and slower jets with *We* from 15 to 35. In the case of the slurry jets, *We* is also a function of the loading through the density due to the solid phase as well as the velocity. Fig. 8 shows a high *We* slurry jet where the density is 1.17 g/cm^3 and the volume of particles is 8.5% of the total. Small-amplitude nonsymmetric waves may be seen on the surface at the top of the photograph. These bear no simple relationship to the imposed disturbance wavelength and are nonaxisymmetric. Farther downstream, more symmetric, longer wavelength waves begin to form, but the distance between the necks is not uniform, and the growth of the waves is not monotonic. The growth of the waves on the high *We* slurry jet is far more complex than for liquids. The jet shape is due to the regular mode of breakup caused by the nozzle oscillation with secondary random disturbances superimposed on it. Because of the irregularities of the high

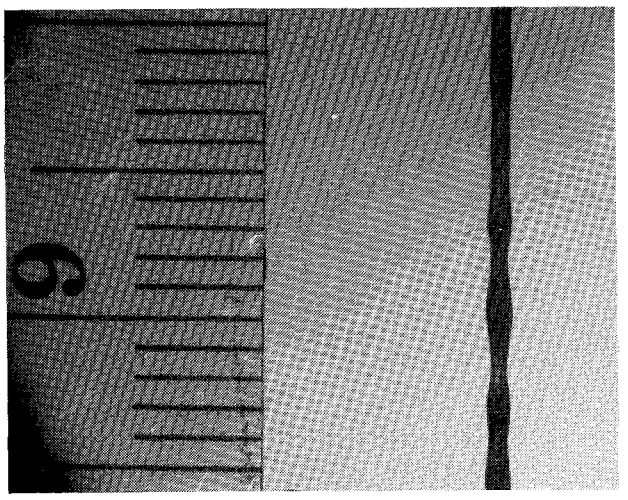

Fig. 8 Slurry jet. $V_0 = 330$ cm/s, $\ell = 1.17$ g/cm^3, $We = 130$, $f = 1000$ Hz, $\lambda/D_0 = 4.3$.

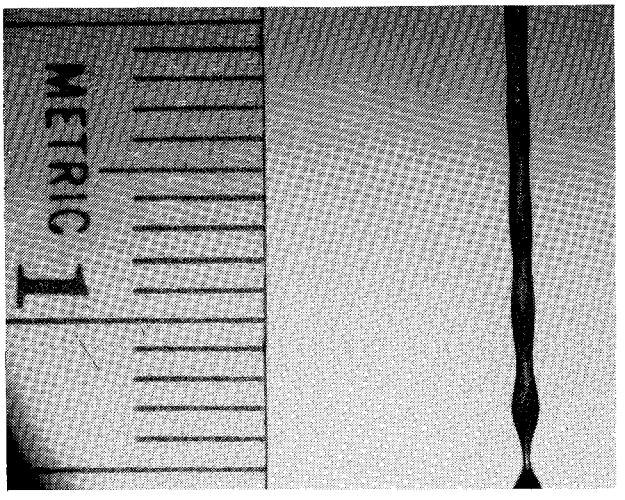

Fig. 9 Slurry jet. $V_0 = 142$ cm/s, $\ell = 1.10$ g/cm^3, $We = 16$, $f = 431$ Hz, $\lambda/D_0 = 4.5$.

We slurry jet, no meaningful growth rate measurements could be determined.

The method used to improve the uniformity of slurry jet breakup was reduction of the initial velocity, but, if the velocity is reduced too far, adhesion of the liquid to the nozzle causes the fluid to simply "drip" from the nozzle forming no continuous fluid column. A low Weber number regime of reasonably regular jet behavior was found for $15 \leq We \leq 40$. Figure 9 shows a typical low *We* slurry jet. The jet is flattened slightly on the right-hand side, and slurry particles or clumps of particles are visible on the jet. The axial symmetry of the jet improves at the higher amplitude disturbances, and the shape of the wave also is more sinusoidal in this group.

The slurry jets all have small irregular disturbances which will grow if the imposed disturbance is not of sufficient amplitude to suppress these background disturbances. There are nonaxisymmetric modes of disturbance growth, some of which appear helical in form. These have also been found in other studies with liquid jets (see Refs. 9 and 10.) There also may be "buckling" similar to Euler buckling of solid columns. This has been discussed for liquid jets in Ref. 11. Herein we have concentrated mainly on the behavior of axisymmetric modes.

Based on our best judgment, the growth of the nearly axisymmtric disturbances on the jet in Fig. 9 is plotted in Fig. 10. The growth rate is nearly exponential for both the neck and the swell, and the growth rate of the neck increases with time. Comparing these results to those for a liquid jet at a similar λ/D_0 and *We,* one finds that the growth rates for the swells are nearly the same. The swell and neck show similar growth on the slurry jet, while on the liquid jet the growth rates are different and the growth rate for the neck is rapidly changing.

The jet in Fig. 11 has a disturbance wavelength of 3.9 diam and $We = 17$. The waves are quite regular, and the large amplitude waves are nearly sinusoidal. A single satellite drop may be seen, and it is similar in size to the satellites on the liquid jet in Fig. 6 where the disturbance wavelength is 3.8 diam. Comparing the corresponding measurements in Figs. 12 and 7, the average growth rate is seen to be quite similar for both jets. In both cases, the swells lag the necks. The growth rate exponent is increasing with time for the swells, and increases more rapidly for the slurry than for the liquid. For both the liquid and the slurry, the growth rate of the necks remains nearly constant.

Numerical Predictions

The initial surface perturbation is assumed as a half sinusoid of amplitude 0.0005 diameter with the crest at the center of the incipient drop and the trough at the center of the neck. Initially, the jet is of uniform pressure with a small surface perturbation. This creates pressure discontinuities

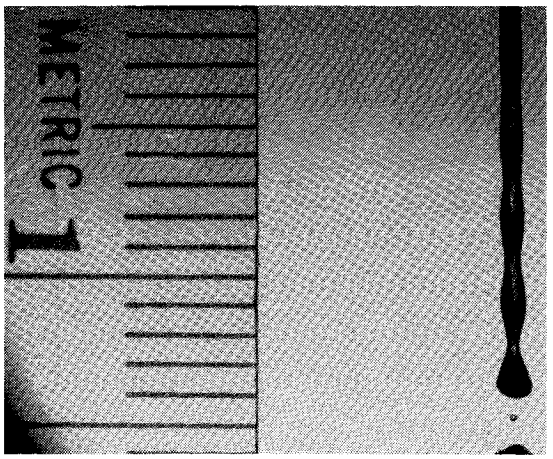

Fig. 11 Slurry jet. $V_0 = 122$ cm/s, $\ell = 1.10$ g/cm^3, $We = 17$, $f = 431$ Hz, $\lambda/D_0 = 3.9$.

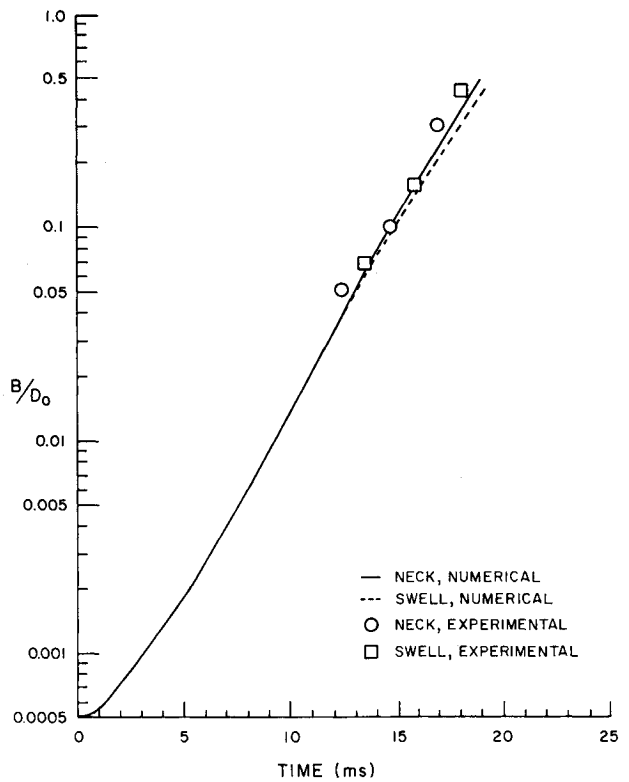

Fig. 10 Predicted nondimensional disturbance amplitude as a function of time compared to experimental results for a slurry jet. The numerical prediction is for $\lambda/D_0 = 4.51$, $\ell = 1.1$ g/cm^3. The experimental conditions are for the jet in Fig. 11, $\lambda/D_0 = 4.5$.

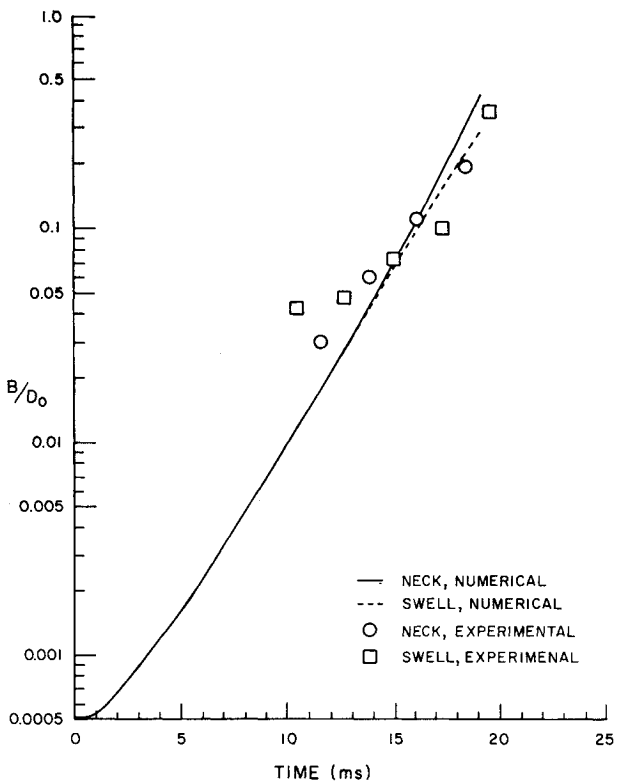

Fig. 12 Predicted nondimensional disturbance amplitude as a function of time compared to experimental results for slurry jets. Numerical prediction is for $\lambda/D_0 = 3.9$, $\ell = 1.1$ g/cm^3. Experimental results are from the jet in Fig. 13, $\lambda/D_0 = 3.9$.

near the surface which take some time to diffuse throughout the flowfield. The initial perturbation is a surface disturbance, not a velocity or pressure disturbance such as in the experiments. There is no characteristic Weber number here because the initial mean velocity of the fluid is taken to be zero. The end conditions are that of a free-slip wall and the surface of the fluid is assumed normal to the wall.

The results for the liquid cases are the velocity, pressure, and volume fraction of fluid in each cell vs time. Results for the slurry included the velocity of the particle phase and local particle phase density in each cell. The position and orientation of the fluid surface then can be computed for plotting. From that the dimensions of the necks and swells can be determined. The method of determining the wave growth rate is then quite similar to that for the experiments, i.e., the minimum and maximum diameter are used for the necks and swells. The amplitude was plotted against time on a semilog graph for comparison with the experimental observations. The boundary conditions limit the instabilities of the jet to axisymmetric modes.

The first results and comparisons with data are for two liquid cases. The prediction for the growth of the surface disturbances have been given previously in Figs. 4 and 5 along with the measurements. Earlier, it was stated that the time scale shown was reckoned relative to a "shifted" origin. This is because the initial imposed disturbance of the jet is not exactly the same in the experiments and calculations. Indeed, the precise details of the very small initial disturbances in the experiments are unknown except for the frequency. Thus, in order to compare the predictions and experiments on a rational basis, it is necessary to make an assumption. We have chosen to assume that by the time the disturbances grow to about 10% of the initial diameter, the effects of the mismatch in the initial disturbances will be minimal. In particular, we shifted the origin for time so that the measurements and predictions were in agreement when the amplitude of the neck disturbance was 0.10. For the calculation, a sharp initial curvature of the growth curve is seen. This is due to the diffusion of the initial pressure discontinuity from the initial surface perturbation.

The surface disturbance growth predicted by the numerical calculation is excellent in all details compared to the experiment. The magnitude and direction of the differences between the behavior of the necks and swells is modeled very well.

The graphs in Fig. 13 show predictions of the jet surface at a series of times up to breakoff. The swell of the wave is on the extreme left of the graph, and on the right is the neck of the initial wave, even though at advanced times as the satellite drop grows, this becomes the swell of the satellite droplet. Thus, the graph shows one-half of a total wavelength. The waveform is almost straight at the initial time, but after 11.7 ms, the amplitude of the disturbance can clearly be seen. At 17.8 ms, the waveform is visibly deviating away from the sinusoid. At more advanced times, the formation of the incipient satellite drop can be seen, and by 18.7 ms, separation has occurred and the drop and satellite are separate. Comparing the graphs in Fig. 13 with the photo in Fig. 3, the close similarity between the numerical and experimental results can be seen. The shape and length of the necks are similar. The observed incipient drops are slightly larger toward their downstream end, but the numerical boundary conditions do not allow for these phenomena. Also, the experiment shows that the disturbance is not quite symmetric about the jet axis, and the numerical boundary conditions do not allow for these effects.

In general, the numerical analysis predicts the behavior of the growth of the surface waves very well. The half-wave computational grid and the symmetric boundary conditions provide good approximations of the experimental case. The nonlinear features of the surface tension driven wave growth at large disturbance amplitudes are clearly well modeled. The breakoff of the drop and satellite formation of the experiments is predicted.

The curves on Fig. 5 show the predicted nondimensional disturbance amplitude growth compared to experiment for $\lambda/D_0 \approx 4.5$. At larger disturbance amplitudes, the numerical method predicts that the necks grow somewhat faster than the swells, but the experimental results indicate that the necks and swells grow at nearly the same rate.

Next, we turn to predictions for slurry jets. The predictions shown in Fig. 14 are for the slurry jet in Fig. 9. The predicted waveform is smooth and nearly sinusoidal up to 17.2 ms. At 18.0 ms, a long ligament can be seen forming which by 19.0 ms has broken and formed a satellite droplet. This ligament formation is also seen in Fig. 9.

The curves on Fig. 10 show the predicted growth rate for the same case. The predicted growth of the necks is slightly faster than that of the swells at larger disturbance amplitudes. Comparing the predictions to the data, it can be seen that the general agreement is good for both neck and swell behavior and the general growth rate, except at the highest amplitude disturbances. In this region, the numerical method slightly underpredicts the growth rate and overpredicts the difference between the neck and the swell.

The predictions for the slurry case with $\lambda/D_0 = 3.9$ shown in Fig. 11 are shown as curves on Fig. 12. Both the predictions and the data show a larger difference between the behavior of the necks and swells than for the previous case at $\lambda/D_0 \approx 4.6$. However, the difference in the experiments is larger than predicted. The data for the swells behave somewhat erratically. Also, the predicted growth rate appears to be higher than observed, as shown most clearly by comparing prediction and data for the necks. Comparing the predicted instantaneous shapes of this jet (not given here due to space limitations) with the photo one finds that the ligament length and satellite size are overpredicted. This case is for $\lambda/D_0 \approx 3.9$ which is not very near the 4.51 value for a predicted maximum

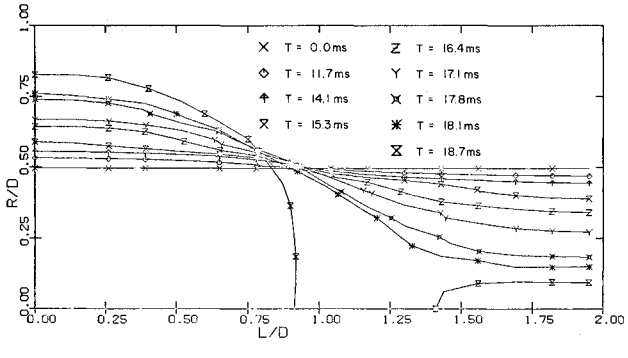

Fig. 13 Graph of the predicted surface shape for a liquid jet. $\lambda/D = 3.9$.

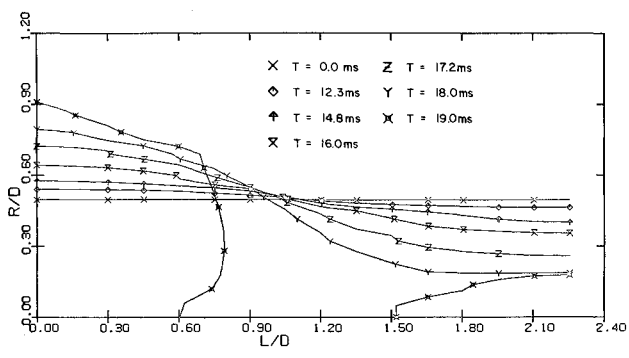

Fig. 14 Graph of the predicted surface shape for a slurry jet. $\lambda/D_0 = 4.51$, $\ell' = 1.1$ g/cm^3.

initial growth rate of axisymmetric disturbances, therefore, the other modes of disturbance growth discussed earlier may play a more prominent role.

Conclusions

The following general conclusions can be made from this investigation.

1) The initial conditions and disturbance amplitude have a strong influence on the growth of the disturbances. The initial perturbations in experiments of jets issuing from vibrating nozzles are primarily velocity disturbances. This affects wave growth at very early times when surface tension effects are small and near the time of breakoff.

2) The numerical prediction models the nonlinear behavior of the capillary jet accurately. The initial conditions chosen for the numerical calculatons are not exactly the same as those of the experiments, and this may affect satellite formation. The boundary conditions of the numerical prediction restrict the development of any nonaxisymmetric disturbances which are permitted to grow during the experiments.

3) The basic effect of the addition of a solid phase to the breakup of slurry jets is to decrease the growth rate of the disturbance; the effect is correctly modeled by the numerical predictions for slurries of low density. Perhaps most importantly, the addition of a solid phase greatly enhances the development of nonaxisymmetric surface disturbances.

4) The numerical prediction has least success modeling the slurry during the very early and late stages of wave growth, indicating that these growth regions are most strongly affected by the initial conditions which are not completely modeled by the numerical boundary and initial conditions.

Acknowledgment

This work was supported by the Air Force Office of Scientific Research with Dr. B. T. Wolfson as the Technical Monitor.

References

[1] Olson, W. T. and Setze, P. C., "Some Combustion Problems of High-Energy Fuels for Aircraft," *Seventh Symposium (International) on Combustion,* Butterworth Scientific Publications, 1959, pp. 883-889.

[2] Rayleigh, Lord, *Theory of Sound,* MacMillian, London, Vol. 2, 1896; reprinted by Dover Press, N.Y., 1945.

[3] Chandrasekhar, S., *Hydrodynamic and Hydromagnetic Stability,* 1961, Clarendon Press, London, England, republished by Dover Publications, N.Y., 1981.

[4] Bogy, C.B., "Drop Formation in a Circular Liquid Jet," *Annual Review of Fluid Mechanics,* Vol. 11, Annual Reviews Inc., Palo Alto, Calif. 1979, pp. 207-228.

[5] Shokoohi, F., "Numerical Investigation of the Disintegration of Liquid Jets," Ph.D. Dissertation, Columbia University, N.Y., 1976.

[6] Harlow, F. H. and Welch, J. E., "Numerical Calculation of Time-Dependent Viscous Incompressible Flow of Fluid with Free Surface," *Physics of Fluids,* 1965, Vol. 8, No. 12, pp. 2182-2188.

[7] Hirt, C. W. Nicholas, B. D., and Romero, N. C., "SOLA-VOF: A Solution Algorithm for Transient Fluid Flow with Multiple Free Boundaries," Los Alamos Scientific Laboratory, New Mexico, Rept. LA-8355, 1980.

[8] Soo, S. L., *Fluid Dynamics of Multiphase Systems,* Blaisdell, Waltham, Maine, 1967.

[9] Batchelor, G. K. and Gill, A. E., "Analysis of the Stability of Axisymmetric Jets," *Journal of Fluid Mechanics,* Vol. 14, Part 4, Dec. 1962, pp. 529-531.

[10] Reynolds, A. J., "Observations of a Liquid-into-Liquid Jet," *Journal of Fluid Mechanics,* Vol. 14, Part 4, 1962, pp. 552-556.

[11] Stockman, M. G. and Bejan, A., "The Nonaxisymmetric (Buckling) Flow Regime of Fast Capillary Jets," *Physics of Fluids,* Vol. 25, Sept. 1982, pp. 1506-1511.